

MEASUREMENT-ALIGNED SAMPLING FOR INVERSE PROBLEMS

Anonymous authors

Paper under double-blind review

ABSTRACT

Diffusion models provide a powerful way to incorporate complex prior information for solving inverse problems. However, existing methods struggle to correctly incorporate guidance from conflicting signals in the prior and measurement, and often failed to maximizing the consistency to the measurement, especially in the challenging setting of non-Gaussian or unknown noise. To address these issues, we propose Measurement-Aligned Sampling (MAS), a novel framework for linear inverse problem solving that flexibly balances prior and measurement information. MAS unifies and extends existing approaches such as DDNM, TMPD, while generalizing to handle both known Gaussian noise and unknown or non-Gaussian noise types. Extensive experiments demonstrate that MAS consistently outperforms state-of-the-art methods across a variety of tasks, while maintaining relatively low computational cost.

1 INTRODUCTION

Inverse problems are prevalent in image restoration (IR) tasks, including super-resolution, inpainting, deblurring, colorization, denoising, and JPEG restoration (Chung et al., 2022a; Kawar et al., 2022a; Saharia et al., 2022; Wang et al., 2022; Lugmayr et al., 2022; Mardani et al., 2023; Song et al., 2023b; Kawar et al., 2022b). Solving an inverse problem involves recovering an unknown original image $x_0 \in \mathbb{R}^n$ based on information from a prior distribution, $\pi(x_0)$, and noisy measurements $y \in \mathbb{R}^m$ generated through a forward model:

$$y = \mathcal{H}(x_0) + \epsilon. \quad (1)$$

Here $\epsilon \in \mathbb{R}^m$ represents measurement noise, $x_0 \in \mathbb{R}^d$ is drawn from data distribution $\pi_0(x_0)$, $\mathcal{H} : \mathbb{R}^d \mapsto \mathbb{R}^m$ is the measurement function, and $y \in \mathbb{R}^m$ denotes the degraded measurement or observed image. A useful motivating example is a high-resolution image x_0 , with a noisy degraded image y and a known corruption process.

Pretrained diffusion and flow models offer a prior distribution $\pi_0(x_0)$ that greatly aids in solving inverse problems. Methods such as DPS (Chung et al., 2022a), IIGDM (Song et al., 2023b), and TMPD (Boys et al., 2023) estimate conditional scores directly from the measurement model by leveraging score decomposition to guide each diffusion sampling step. In contrast, approaches like FPS (Dou & Song, 2024), DAPS (Zhang et al., 2024), MPGD (He et al., 2023), and optimization-based methods (Song et al., 2023a; Zhu et al., 2023; Li et al., 2024; Wang et al., 2024) align denoiser outputs directly with measurements, thereby avoiding backpropagation through the U-Net. Although DAPS achieves state-of-the-art performance—outperforming methods that require backpropagation—it still requires more than 100 gradient descent iterations per diffusion step, making it far more computationally expensive compared to methods such as DDNM (Wang et al., 2022) and DDRM (Kawar et al., 2022a). This highlights the promise of developing approaches that avoid both backpropagation through U-Net and excessive optimization steps, while still attaining state-of-the-art performance.

Moreover, the above approaches lack the ability to effectively handle unknown or non-Gaussian noise. In practical settings, noise frequently deviates from Gaussian assumptions—exhibiting characteristics like salt-and-pepper, periodic, or Poisson distributions—or is completely unknown. Additionally, the forward measurement operator may be uncertain or inaccurately specified. Effectively addressing

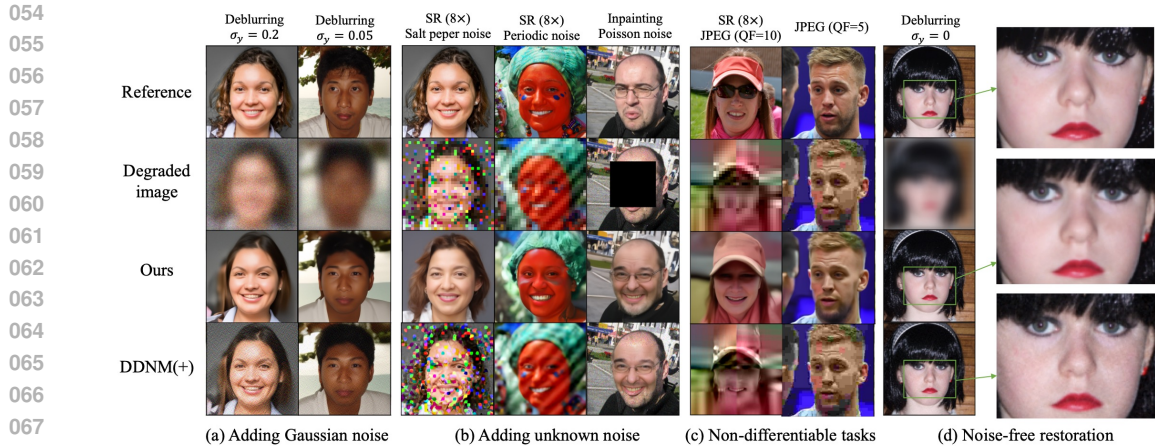


Figure 1: Solving various inverse problems using unconditional diffusion models. Our model demonstrates better robustness with unknown noise and strong Gaussian noise.

Table 1: Comparison of method applicability across different inverse problems.

Inverse Problem	Noise strength	DDNM	DDRM	IIGDM	DAPS	RED-Diff	MAS (ours)
Linear + noise free	-	✓	✓	✓	✓	✓	✓
Linear + Gaussian noise	Known	✓	✓	✓	✓	✓	✓
Linear + non-Gaussian noise	Unknown	✗	✗	✗	✗	✗	✓
JPEG / Quantization restoration	Known	✗	✗	✓	✗	✗	✓
JPEG / Quantization restoration	Unknown	✗	✗	✗	✗	✗	✓

inverse problems under these more general and realistic conditions remains an open and challenging research area.

Our main contributions are summarized as follows:

- We propose *Measurement-Aligned Sampling* (MAS), a novel framework for solving linear inverse problems. MAS provides both probabilistic and optimization perspectives and generalizes approaches such as DDNM and TMPD for linear inverse problems. Furthermore, our proposed ‘overshooting’ technique achieves superior restoration quality compared to DDNM across various inverse problem scenarios.
- We develop new techniques that *maximize consistency with the measurement*, enabling robust handling of both Gaussian noise and unknown noise sources. Moreover, our novel parameterization scheme allows us to effectively handle noisy inverse problems with unknown or non-Gaussian noise structures and even non-differentiable measurements, such as JPEG restoration, without requiring explicit knowledge of the forward operator or noise level. The comparison of method applicability across different inverse problems is shown in Table 1.
- Our experiments show that MAS enables robust and efficient image restoration, consistently outperforming baselines across Gaussian, non-Gaussian, and non-differentiable degradations (see Fig. 1 and experiments in Sec. 5).

2 BACKGROUND

Given training dataset $\mathcal{D} = \{x_0^i\}_{i=1}^N$ from target distribution $\pi_0(x_0)$, $x_0^i \in \mathbb{R}^d$, the goal of generative modeling is to draw new samples from π_0 . In the context of conditional generation, suppose that we have data samples from a joint distribution $(x_0^i, y) \sim \pi(x_0, y)$, where x_0, y are dependent, and y could be class labels or text information, for example.

For conditional generative modeling, we seek to draw new samples from $\pi(x_0 | y)$ for a given condition y . Conditioned flows (Zheng et al., 2023) build a marginal probability path $p_{t|y}$ using a

mixture of interpolating densities: $p_{t|y}(x_t | y) = \int p_t(x_t | x_0)\pi(x_0 | y)dx_T$, where $p_t(\cdot | x_0)$ is a probability path interpolating between noise and a single data point x_T . In general, the conditional kernel $p_t(x_t | x_0)$ is given by a Gaussian distribution: $p_t(x_t | x_0) = \mathcal{N}(x_t; \alpha_t x_0, \sigma_t^2 \mathbb{I})$, where \mathcal{N} is the Gaussian kernel, α_t, σ_t are differentiable functions. Then we can sample from the conditional distribution $p_{0|y}(x_0 | y)$ by simulating a stochastic process $p_{t|y}(x_t | y)$ from time $t = T$ to $t = 0$. Although different sampling methods can be chosen, generally, the iteration follows the form:

$$x_{t-\Delta t} \sim \mathcal{N}(a_t m_{0|t,y} + b_t x_t, c_t^2 \mathbb{I}). \quad (2)$$

where $m_{0|t,y} = \mathbb{E}[x_0 | x_t, y]$ is the ideal conditional denoiser, a_t, b_t and c_t are parameters that depends on samplers. For instance, $x_{t-\Delta t} \sim \mathcal{N}(\alpha_{t-\Delta t} m_{0|t,y}, \sigma_{t-\Delta t}^2 \mathbb{I})$ is a valid DDIM sampler. In the implementation of conditional diffusion models, a denoiser is trained to approximate $m_{0|t,y}$. However, when only an unconditional denoiser $m_{0|t} = \mathbb{E}[x_0 | x_t]$ is available, training-free conditional inference methods are employed.

Diffusion Posterior Sampling (DPS) and its variants. Given unconditional denoiser $\mathbb{E}[x_0 | x_t]$, training-free conditional inference methods enable the approximation of the ideal conditional denoiser $\mathbb{E}[x_0 | x_t, y]$ (Pokle et al., 2023):

$$\mathbb{E}[x_0 | x_t, y] = \mathbb{E}[x_0 | x_t] + \frac{\sigma_t^2}{\alpha_t} \nabla_{x_t} \log p(y | x_t). \quad (3)$$

Since $\nabla_{x_t} \log p(y | x_t)$ is generally intractable, various approaches have been developed to approximate it, such as heuristic approximation (Fei et al., 2023).

For linear inverse problems, where the forward model is given by: $y = Hx_0 + \epsilon$, $\epsilon \sim \mathcal{N}(0, \sigma_y^2 \mathbb{I})$. Tweedie Moment Projected Diffusion (TMPD) (Boys et al., 2023) provides a more accurate approximation. TMPD assumes $p(x_0 | x_t)$ as a Gaussian: $p(x_0 | x_t) \approx \mathcal{N}(m_{0|t}, C_{0|t})$, where $m_{0|t}(x_t) := \mathbb{E}[x_0 | x_t]$ is the ideal unconditional denoiser, $C_{0|t}(x_t) := \mathbb{E}[(x_0 - m_{0|t})(x_0 - m_{0|t})^T | x_t]$ is the covariance of $x_0 | x_t$. Then the posterior mean $\mathbb{E}[x_0 | x_t, y]$ admits an explicit closed-form solution:

$$\mathbb{E}[x_0 | x_t, y] = m_{0|t} + C_{0|t} H^T (H C_{0|t} H^T + \sigma_y^2 \mathbb{I})^{-1} (y - H m_{0|t}) \quad (4)$$

The covariance $C_{0|t}$ could be calculated via gradient go through the denoiser: $C_{0|t} = \frac{\sigma_t^2}{\alpha_t} \nabla_{m_{0|t}}(x_t)$. Since calculating the gradient with respect to $m_{0|t}$ is time-consuming, Yismaw et al. (2025) and Peng et al. (2024) try to find the optimal isotropic approximation of $C_{0|t}$, i.e., $C_{0|t} \approx r_t^2 \mathbb{I}$.

Optimization based methods. Unlike DPS guarantees that sampling is strictly from the conditional distribution, $p(x_0 | y)$, optimization-based approaches (Zhu et al., 2023; Li et al., 2024; Wang et al., 2024) place more emphasis on the alignment with the measurement and the prior, which takes the following iteration:

$$x_0^* = \arg \min_{x_0} \|x_0 - m_{0|t}\|^2 + \frac{1}{\eta_t} \|y - \mathcal{H}(x_0)\|^2, \quad (5a)$$

$$x_{t-\Delta t} \sim \mathcal{N}(a_t x_0^* + b_t x_t, c_t^2). \quad (5b)$$

where η_t is a manually designed hyperparameter and $\mathcal{H}(\cdot)$ is the nonlinear forward operator. The iteration of optimization based methods could be seen as replacing $m_{0|t,y}$ in Eq. (2) to x_0^* in Eq. (5a).

3 METHODOLOGY

For optimization based methods, the data-consistency loss with respect to the measurement y is treated uniformly across all directions of the measurement space. However, for inverse problems it is often advantageous to introduce a weighting matrix that reflects the geometry of the forward operator (Tarantola, 2005). To this end, we propose Measurement-Aligned Sampling (MAS), which incorporates such a weighting into the optimization. As we demonstrate in Sec. 5, this alignment leads to significant improvements in reconstruction quality.

Algorithm 1 Measurement-Aligned Sampling (MAS) for inverse problems.

```

1: Input: measurement  $y$ , forward operator  $H(\cdot)$ , pretrained DM  $\epsilon_\theta(\cdot)$ , number of diffusion step  $N$ , diffusion
   schedule  $\alpha_t$  and  $\sigma_t$ , objective parameters  $\eta_1, \eta_2$ .
2: Initialization:  $x_N \sim \mathcal{N}(0, \mathbb{I})$ 
3: for  $n = N$  to 1 do
4:    $\hat{x}_0 \leftarrow [x_n - \sigma_n \epsilon_\theta(x_n, n)] / \alpha_n$  ▷ Obtain predicted data  $\mathbb{E}[x_0 | x_n]$ 
5:    $x'_0 = Y^{-1}[\hat{x}_0 + H^\top W^{-1} y]$  ▷ Calculating posterior mean  $\mathbb{E}[x_\epsilon | x_n, y]$ 
6:    $x_{n-1} \sim \mathcal{N}(\alpha_{n-1} x'_0, \sigma_{n-1} \mathbb{I})$  ▷ Forward diffusion step
7: end for
8: Output  $x_0$ 

```

3.1 MEASUREMENT ALIGNED SAMPLING

In this work, we generalize the objective in Eq. (5a) as

$$x_0^* = \arg \min_{x_0} \|x_0 - m_{0|t}\|^2 + \|y - Hx_0\|_{W^{-1}}^2. \quad (6)$$

where $W := \eta_1 HH^\top + \eta_2 \mathbb{I}$ (with $\eta_1 \geq 0, \eta_2 \geq 0$) is the weighted matrix and serves as a metric that balances measurement fidelity and prior regularization, where $\|z\|_A^2 = z^\top Az$.

η_1 and η_2 are the primary hyperparameters of MAS that need to design. When $\eta_1 = 0$ and $\eta_2 > 0$, corresponding to the classical Tikhonov (ridge) regularization, where η_2 controls the trade-off between fitting the measurements y and staying close to the prior $m_{0|t}$. When $\eta_1 > 0$ and $\eta_2 = 0$, the data term becomes weighted by $(HH^\top)^{-1}$, a Mahalanobis-type distance that emphasizes alignment along directions where H is weak (small singular values), thereby regularizing ill-posed components of the inverse problem. *The balance between η_1 and η_2 is crucial for reconstruction performance*, as we show in our experiments.

Finally, Eq. (6) admits a unique closed-form solution obtained by setting the gradient to zero:

$$x_0^* = Y^{-1}[m_{0|t} + H^\top W^{-1} y] \quad (7)$$

where $W := \eta_1 HH^\top + \eta_2 \mathbb{I}, \quad Y := \mathbb{I} + H^\top W^{-1} H,$

In practice, computing the inverse W^{-1} and Y^{-1} in Eq. (7) naively can be computationally expensive. Instead, one can employ singular value decomposition (SVD) for more efficient computation; see Sec. B.2 for details.

Remark 1 (Connection with DDNM (Wang et al., 2022)). As $\eta_2 = 0$ and $\eta_1 \rightarrow 0$, $x_0^* \rightarrow \tilde{x}_0^{\text{DDNM}} := m_{0|t} + H^\dagger(y - Hm_{0|t})$. Thus, in this limiting case, MAS recovers DDNM.

Remark 2 (Connection with optimization methods). For the case where $\eta_1 = 0, \eta_2 > 0$, Eq. (6) reproduces optimization approaches, such as Resample (Song et al., 2023a), DiffPIR (Zhu et al., 2023), DCDP (Li et al., 2024), DMPlug (Wang et al., 2024).

3.2 PROBABILISTIC INTERPRETATION

We can interpret x_0^* in Eq. (7) as $\mathbb{E}[x_\epsilon | x_t, y]$, where $x_\epsilon \approx x_0$ with perturbation variance σ_ϵ^2 chosen to be sufficiently small so that $p(x_0 | x_\epsilon) \approx \mathcal{N}(x_\epsilon, \sigma_\epsilon^2 \mathbb{I})$. Given the measurement model $p(y | x_0) = \mathcal{N}(Hx_0, \sigma_y^2 \mathbb{I})$ and conditional $p(x_0 | x_\epsilon) = \mathcal{N}(x_\epsilon, \sigma_\epsilon^2 \mathbb{I})$, the induced distribution over the measurement conditioned on x_ϵ takes the explicit form:

$$p(y | x_\epsilon) = \mathcal{N}(Hx_\epsilon, \sigma_y^2 \mathbb{I} + \sigma_\epsilon^2 HH^\top). \quad (8)$$

Notably, the likelihood $p(y | x_\epsilon)$ shares the same mean as $p(y | x_0)$, but with a generalized variance inflated by a term depending on H . Since both $p(y | x_\epsilon)$ and $p(y | x_0)$ are Gaussian, the posterior distribution admits a closed-form expression. In particular, the posterior mean $\mathbb{E}[x_0 | x_t, y]$ can be computed via Bayesian linear regression, as stated in Prop. 3.1.

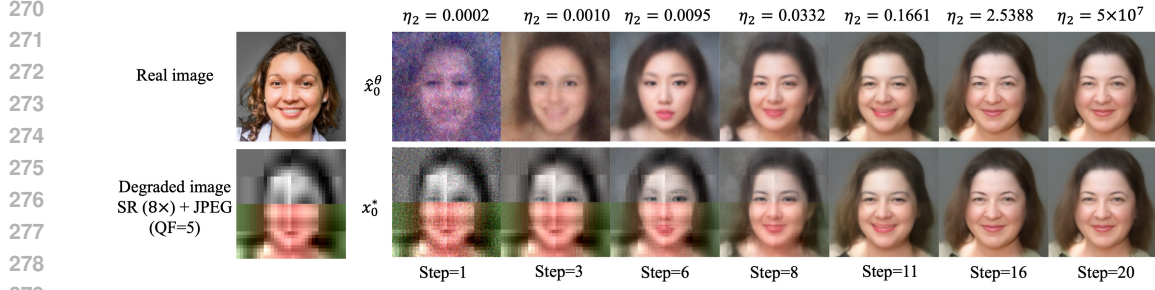


Figure 3: The sample process of solving inverse problems with unknown noise, where $\hat{x}_0^\theta \approx m_{0|t}$ is the denoising output. Here we set $\eta_1 = 0$ and $\eta_2 = 0.5a_t/c_t$.

$$x_0^* = m_{0|t} + \lambda_t \frac{y - m_{0|t}}{\eta_1 + \eta_2 + 1}, \quad x_{t-\Delta t} \sim \mathcal{N}(a_t \tilde{x}_0 + b_t x_t, \gamma_t \mathbb{I}). \quad (11)$$

Here λ_t and γ_t are two parameters that can control the total noise introduced to $x_{t-\Delta t}$. In our work, we adopt similar two principles as DDNM+ (Wang et al., 2022) for handling Gaussian noise: (i) the total noise introduced in $x_{t-\Delta t}$ should be $\mathcal{N}(0, c_t^2 \mathbb{I})$ to conform to the correct distribution of $x_{t-\Delta t}$ in Eq. (2); (ii) λ_t should be as close to 1 as possible to maximize the preservation of x_0^* . As $\epsilon_y \sim \mathcal{N}(0, \sigma_y^2 \mathbb{I})$, principle (i) and principle (ii) are equivalent to:

$$\left(\frac{a_t \lambda_t \sigma_y}{\eta_1 + \eta_2 + 1} \right)^2 + \gamma_t = c_t^2, \quad \lambda_t = \begin{cases} 1, & c_t \geq \frac{a_t \sigma_y}{\eta_1 + \eta_2 + 1} \\ \frac{c_t (\eta_1 + \eta_2 + 1)}{a_t \sigma_y}, & c_t < \frac{a_t \sigma_y}{\eta_1 + \eta_2 + 1} \end{cases}. \quad (12)$$

Derivations for more general forms of H can be found in Sec. B. **Note that the revision does not introduce additional parameters.**

4.3 ADDRESSING UNKNOWN NOISE AND NON-DIFFERENTIABLE MEASUREMENTS

Addressing unknown noise or non-Gaussian noise. When the measurement noise σ_y is non-Gaussian or unknown, it becomes difficult to ensure that the total noise in $x_{t-\Delta t}$ follows the desired distribution $\mathcal{N}(0, c_t^2 \mathbb{I})$. To address this, we continue to sample $x_{t-\Delta t}$ using Eq. (2). Next, the noise introduced to $x_{t-\Delta t}$ is the sum of two components:

$$\epsilon_{\text{ng}} = (a_t \lambda_t \epsilon_y) / (\eta_1 + \eta_2 + 1), \quad \epsilon_g \sim \mathcal{N}(0, c_t^2 \mathbb{I}). \quad (13)$$

Here ϵ_{ng} is related to the noise introduced by unknown noise ϵ_y , while ϵ_g is the noise added by the diffusion process. To minimize the effect of unknown noise ϵ_{ng} , it is desirable for $\eta_1 + \eta_2 + 1$ to be sufficiently large. However, smaller values of η_1 and η_2 result in better consistency with the measurement y , as illustrated in Fig. 2. To balance this trade-off, we propose using a small $\eta_1 + \eta_2$ during the early stages of sampling to fully exploit measurement information. As sampling progresses, $\eta_1 + \eta_2$ should be gradually increased to suppress the impact of ϵ_{ng} . The underlying intuition is that, in the early sampling stage, x_t is still highly noisy and $a_t \approx 0$, so the influence of ϵ_{ng} is negligible even when $\eta_1 + \eta_2$ is small. As shown in Fig. 3, x_0^* is initially more aligned with the degraded observation, but progressively shifts toward $m_{0|t}$ as sampling evolves.

For a general degradation operator H , we recommend setting $\eta_2 = ka_t/c_t$, where k is a constant determined by the characteristics of the introduced noise. The rationale behind this design choice is further detailed in Sec. B.

Addressing non-differentiable measurements. For solving inverse problems with non-differentiable measurements such as JPEG restoration and quantization, the degraded images can be viewed as "noisy images" with unknown noise, modeled by $y = x + \epsilon_y$. In these scenarios, our proposed strategy naturally extends by treating the unknown degradations as implicit noise.

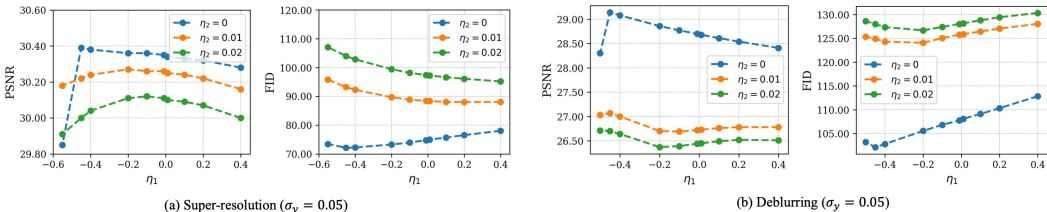


Figure 4: Ablation study of η_1 and η_2 on solving super-resolution and deblurring. We set NFE=20 for all tasks.

5 EXPERIMENTS

5.1 EXPERIMENTAL SETUP

Dataset. We evaluate the effectiveness of our proposed approach on FFHQ 256×256 (Karras et al., 2019) and ImageNet 256×256 (Deng et al., 2009). Following DAPS (Zhang et al., 2024), we test on the same subset of 100 images for both datasets.

Pretrained models and baselines. We utilize the pre-trained checkpoint (Chung et al., 2022a) on the FFHQ dataset and the pre-trained checkpoint (Dhariwal & Nichol, 2021) on the Imagenet dataset. We compare our methods with the following baselines: DCDP (Li et al., 2024), FPS (Dou & Song, 2024), DiffPIR (Zhu et al., 2023), DDNM (Wang et al., 2022), DDRM (Kawar et al., 2022a), IIGDM (Song et al., 2023b), RedDiff (Mardani et al., 2023), DAPS (Zhang et al., 2024).

Metrics. Following previous work (Chung et al., 2022a; Kawar et al., 2022a), we report Fréchet Inception Distance (FID) (Heusel et al., 2017), Learned Perceptual Image Patch Similarity (LPIPS) (Zhang et al., 2018), Peak Signal-to-Noise Ratio (PSNR), and Structural SIMilarity index (SSIM).

Tasks. (1) We evaluate performance on the following linear inverse problems: super-resolution (bicubic filter), deblurring (uniform kernel of size 9), inpainting (with a box mask), inpainting (with a 70% random mask), and colorization. (2) We consider two unknown noise types: salt-and-pepper noise (10% pixels set randomly to ± 1) and periodic noise (sinusoidal pattern with amplitude 0.2 and frequency 5). (3) We address JPEG restoration with quality factors $QF = 2$ and $QF = 5$. (4). For quantization, we consider the challenging case of 2-bit quantization.

5.2 ABLATION STUDY

Ablation Study on η_1 and η_2 . We conduct ablation studies on parameters η_1 and η_2 using two inverse problems: super-resolution (noise-free, $\epsilon_y = 0$) and deblurring (noisy, $\epsilon_y \sim \mathcal{N}(0, \sigma_y^2 \mathbb{I})$). Results presented in Fig. 4 demonstrate that for noise-free super-resolution, the highest PSNR and lowest FID scores are achieved by setting $\eta_2 = 0$ and a negative $\eta_1 = -0.45$. This indicates that appropriate "overshooting" enhances restoration quality. For the noisy deblurring task, negative η_2 yields an improvement of more than 0.5 in PSNR and a reduction of over 5 in FID, further confirming the benefit of overshooting.

5.3 IMAGE RESTORATION

Inverse problems with Gaussian noise (known variance). Quantitative results for inverse problems with Gaussian noise of known variance are shown in Table 2. MAS consistently demonstrates superior performance across most tasks, notably achieving significantly higher PSNRs. The table summarizes 5 tasks, 4 restoration quality metrics, and 2 datasets, resulting in a total of 40 evaluations. MAS demonstrates superior performance in 29 out of the 40 cases. Notably, MAS achieves improvements of more than 1 dB in 5 out of 10 instances.

Inverse Problems with Non-Gaussian Noise (Unknown Strength). Quantitative evaluations for linear inverse problems with unknown, non-Gaussian noise are presented in Table 3. MAS consistently outperforms baseline methods, highlighting the effectiveness of our approach in handling unknown noise conditions.

Table 2: Quantitative evaluation of solving image restoration FFHQ (left) and ImageNet (right), with Gaussian noise (known variance, $\sigma_y = 0.05$).

Task	Method	FFHQ				ImageNet			
		PSNR \uparrow	SSIM \uparrow	LPIPS \downarrow	FID \downarrow	PSNR \uparrow	SSIM \uparrow	LPIPS \downarrow	FID \downarrow
SR 4 \times	DPS	25.86	0.753	0.269	81.07	21.13	0.489	0.361	106.32
	DDRM	26.58	0.782	0.282	79.25	22.62	0.521	0.324	103.85
	DDNM	28.03	0.795	0.197	64.62	23.96	0.604	0.475	98.62
	DCDP	28.66	0.807	0.178	53.81	–	–	–	–
	FPS-SMC	28.42	0.813	0.204	49.25	24.82	0.703	0.313	97.51
	DiffPIR	26.64	–	0.260	65.77	23.18	–	0.371	106.32
	RED-Diff	28.63	0.748	0.288	126.78	25.43	0.639	0.336	153.37
	DAPS	29.07	0.818	0.177	51.44	25.89	0.694	0.276	83.57
	MAS	30.56	0.865	0.131	61.38	27.20	0.751	0.215	88.61
Inpaint (Box)	DPS	22.51	0.792	0.209	61.27	18.94	0.722	0.257	126.52
	DDRM	22.26	0.801	0.207	78.62	18.63	0.733	0.254	116.37
	DDNM	24.47	0.837	0.235	46.59	21.64	0.748	0.319	103.97
	DCDP	23.89	0.760	0.163	45.23	–	–	–	–
	FPS-SMC	24.86	0.823	0.146	48.34	22.16	0.726	0.208	111.58
	RED-Diff	24.68	0.767	0.175	86.78	21.32	0.728	0.247	123.55
	DAPS	24.07	0.814	0.133	43.10	21.43	0.725	0.214	109.85
	MAS	24.95	0.879	0.082	37.67	21.15	0.817	0.168	95.96
Inpaint (Random)	DPS	25.46	0.823	0.203	69.20	23.52	0.745	0.297	87.53
	DDNM	29.91	0.817	0.121	44.37	31.16	0.841	0.191	63.84
	DCDP	30.69	0.842	0.142	52.51	–	–	–	–
	FPS-SMC	28.21	0.823	0.261	61.23	24.52	0.701	0.316	79.12
	RED-Diff	29.73	0.814	0.200	104.19	27.04	0.753	0.226	92.24
	DAPS	31.12	0.844	0.098	32.17	28.44	0.775	0.135	54.25
MAS	33.10	0.923	0.073	34.75	29.05	0.838	0.113	30.19	
Deblurring (Uniform)	DDNM	26.58	0.704	0.210	68.83	25.69	0.630	0.261	83.63
	DDRM	29.19	0.835	0.172	87.12	26.31	0.711	0.267	118.36
	DAPS	28.92	0.758	0.204	76.57	25.43	0.616	0.293	103.55
	MAS	30.58	0.857	0.174	103.88	26.25	0.700	0.295	141.58
Color	DDNM	24.83	0.868	0.244	85.15	22.57	0.884	0.271	87.48
	DDRM	23.27	0.881	0.250	100.48	21.12	0.819	0.346	103.39
	RED-Diff	24.21	0.785	0.304	107.64	22.18	0.782	0.368	104.40
	DAPS	23.92	0.825	0.263	88.09	22.13	0.830	0.323	89.30
	MAS	24.23	0.919	0.187	72.33	22.66	0.886	0.258	83.17

Table 3: Quantitative evaluation of solving linear inverse problems with non-Gaussian noise (unknown strength).

Task	Method	Salt peper noise				Periodic noise				Poisson noise			
		PSNR \uparrow	SSIM \uparrow	LPIPS \downarrow	FID \downarrow	PSNR \uparrow	SSIM \uparrow	LPIPS \downarrow	FID \downarrow	PSNR \uparrow	SSIM \uparrow	LPIPS \downarrow	FID \downarrow
SR 8 \times	DDNM	13.02	0.289	0.710	377.54	18.61	0.492	0.495	268.36	18.79	0.392	0.653	349.88
	DDRM	16.06	0.506	0.629	351.69	19.74	0.545	0.463	218.38	23.47	0.651	0.417	147.70
	IIGDM	17.36	0.476	0.569	309.73	18.12	0.449	0.434	163.41	17.33	0.315	0.640	300.97
	RED-Diff	14.21	0.357	0.668	342.09	19.47	0.596	0.416	224.07	19.62	0.450	0.636	306.88
	MAS (ours)	20.05	0.605	0.390	129.80	20.10	0.591	0.395	137.57	23.69	0.700	0.304	115.16
Inpaint (Box)	DDNM	15.55	0.248	0.533	247.99	18.60	0.621	0.341	147.80	21.30	0.483	0.350	155.41
	DDRM	20.27	0.599	0.350	142.01	18.74	0.589	0.423	199.14	21.10	0.734	0.263	115.24
	IIGDM	19.30	0.665	0.297	100.07	18.32	0.601	0.349	150.49	22.10	0.551	0.318	131.46
	RED-Diff	15.75	0.287	0.523	255.85	19.13	0.638	0.338	159.99	21.93	0.522	0.339	175.14
	MAS (ours)	22.78	0.723	0.244	90.15	19.13	0.581	0.407	138.56	23.26	0.746	0.253	102.11

Inverse problems with non-differentiable measurements. MAS is also capable of solving inverse problems with non-differentiable measurements, such as JPEG restoration and quantization. Results in Table 4 and Fig. 5 show that MAS achieves state-of-the-art performance without relying on the forward operator or knowledge of the degradation strength.

Computational time analysis. The computational efficiency of MAS is comparable to DDNM and substantially higher than DAPS. For example, on the SR task using the FFHQ-256 dataset with 200 NFEs, the non-parallel single-image sampling time for both DDNM and MAS is only 8 seconds, whereas DAPS requires 67 seconds (test were conducted on the same NVIDIA A6000 GPU).

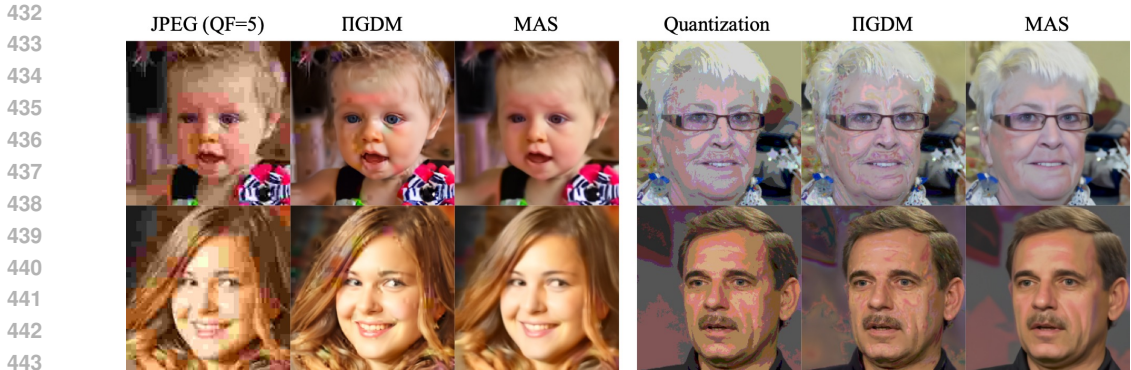


Figure 5: Results on JPEG (QF=5) and quantization restoration.

Table 4: Quantitative evaluation of solving JPEG restoration and Quantization. We set $k = 1.0$ for QF = 5 and $k = 3.0$ for QF = 2, and $k = 0.5$ for quantization. Both PIGDM and MAS use NFE = 20, which yields the best performance (among NFE = 20 and NFE = 100). Notably, our method (MAS) does not require access to the forward operator or the strength of degradation.

Method	JPEG Restoration (QF = 5)				JPEG Restoration (QF = 2)				Quantization (number of bits = 2)			
	PSNR \uparrow	SSIM \uparrow	LPIPS \downarrow	FID \downarrow	PSNR \uparrow	SSIM \uparrow	LPIPS \downarrow	FID \downarrow	PSNR \uparrow	SSIM \uparrow	LPIPS \downarrow	FID \downarrow
PIGDM	25.78	0.750	0.241	89.82	22.92	0.653	0.314	112.27	29.98	0.823	0.185	124.57
MAS (ours)	26.30	0.787	0.281	101.24	23.72	0.772	0.335	114.85	28.97	0.837	0.196	69.61

6 RELATED WORK

Diffusion models have also been successfully applied to linear inverse problems, including, compressed-sensing MRI (CS-MRI), and computed tomography (CT) (Kadkhodaie & Simoncelli, 2021; Song et al., 2020b; Chung et al., 2022b; Kawar et al., 2022a; Song et al., 2021). They have also been extended to non-linear inverse problems such as Fourier phase retrieval, nonlinear deblurring, HDR, and JPEG restoration (Chung et al., 2022a; Song et al., 2023b; Chung et al., 2023; Mardani et al., 2023).

Methods to solve inverse problems include linear projection methods (Wang et al., 2022; Kawar et al., 2022a; Dou & Song, 2024), Monte Carlo sampling (Wu et al., 2023; Phillips et al., 2024), variational inference (Feng et al., 2023; Mardani et al., 2023; Janati et al., 2024), optimization-based approaches (Song et al., 2023a; Zhu et al., 2023; Li et al., 2024; Wang et al., 2024; Alkhouri et al., 2024; He et al., 2023), and Diffusion Posterior Sampling (DPS) (Zhang et al., 2024; Chung et al., 2022a; Song et al., 2023c; Yu et al., 2023; Rout et al., 2024; Yang et al., 2024; Bansal et al., 2023; Boys et al., 2023; Song et al., 2023b; Ho & Salimans, 2022). Besides, InverseBench (Zheng et al., 2025) presents a benchmark for critical scientific applications, which present structural challenges that differ significantly from natural image restoration tasks.

7 CONCLUSION

MAS improves upon existing methods by explicitly aligning the sampling process with measurement data, offering a broader optimization perspective that generalizes approaches like DDNM and DAPS. Beyond the noise-free case, MAS can be extended to: (1) known Gaussian noise, (2) unknown or non-Gaussian noise through adaptive parameterization, and (3) non-differentiable degradations (e.g., JPEG) by decoupling the forward operator from sampling. Extensive experiments show that MAS consistently outperforms state-of-the-art methods across a wide range of inverse problems. While MAS can handle non-differentiable measurements like JPEG restoration, it does not support general non-linear inverse problems, it’s also promising to ‘calibrate’ the noise introduced into x_t , such that maximizing the consistency to measurement.

486 REPRODUCIBILITY STATEMENT
487

488 All code and instructions necessary to reproduce our experiments are anonymously available at
489 https://anonymous.4open.science/r/MAS_linear-8C3C. We provide a PyTorch-
490 like implementation of the calculation of x_0^* in Eq. (7), included in Sec. E.
491

492 ETHICS STATEMENT
493

494 This work does not present any foreseeable ethical issues.
495
496

497 REFERENCES

- 498 Ismail Alkhouri, Shijun Liang, Cheng-Han Huang, Jimmy Dai, Qing Qu, Saiprasad Ravishankar,
499 and Rongrong Wang. Sitcom: Step-wise triple-consistent diffusion sampling for inverse problems.
500 *arXiv preprint arXiv:2410.04479*, 2024.
501
- 502 Arpit Bansal, Hong-Min Chu, Avi Schwarzschild, Soumyadip Sengupta, Micah Goldblum, Jonas
503 Geiping, and Tom Goldstein. Universal guidance for diffusion models. In *Proceedings of the*
504 *IEEE/CVF conference on computer vision and pattern recognition*, pp. 843–852, 2023.
- 505 Benjamin Boys, Mark Girolami, Jakiw Pidstrigach, Sebastian Reich, Alan Mosca, and Omer Deniz
506 Akyildiz. Tweedie moment projected diffusions for inverse problems. *Transactions on Machine*
507 *Learning Research*, 2023.
508
- 509 Hyungjin Chung, Jeongsol Kim, Michael T Mccann, Marc L Klasky, and Jong Chul Ye. Diffusion
510 posterior sampling for general noisy inverse problems. *arXiv preprint arXiv:2209.14687*, 2022a.
- 511 Hyungjin Chung, Byeongsu Sim, Dohoon Ryu, and Jong Chul Ye. Improving diffusion models for
512 inverse problems using manifold constraints. *Advances in Neural Information Processing Systems*,
513 35:25683–25696, 2022b.
514
- 515 Hyungjin Chung, Jeongsol Kim, Sehui Kim, and Jong Chul Ye. Parallel diffusion models of operator
516 and image for blind inverse problems. In *Proceedings of the IEEE/CVF Conference on Computer*
517 *Vision and Pattern Recognition*, pp. 6059–6069, 2023.
- 518 Jia Deng, Wei Dong, Richard Socher, Li-Jia Li, Kai Li, and Li Fei-Fei. Imagenet: A large-scale
519 hierarchical image database. In *2009 IEEE conference on computer vision and pattern recognition*,
520 pp. 248–255. Ieee, 2009.
521
- 522 Prafulla Dhariwal and Alexander Nichol. Diffusion models beat gans on image synthesis. *Advances*
523 *in neural information processing systems*, 34:8780–8794, 2021.
- 524 Zehao Dou and Yang Song. Diffusion posterior sampling for linear inverse problem solving: A
525 filtering perspective. In *The Twelfth International Conference on Learning Representations*, 2024.
526
- 527 Ben Fei, Zhaoyang Lyu, Liang Pan, Junzhe Zhang, Weidong Yang, Tianyue Luo, Bo Zhang, and
528 Bo Dai. Generative diffusion prior for unified image restoration and enhancement. In *Proceedings*
529 *of the IEEE/CVF conference on computer vision and pattern recognition*, pp. 9935–9946, 2023.
- 530 Berthy T Feng, Jamie Smith, Michael Rubinstein, Huiwen Chang, Katherine L Bouman, and
531 William T Freeman. Score-based diffusion models as principled priors for inverse imaging.
532 In *Proceedings of the IEEE/CVF International Conference on Computer Vision*, pp. 10520–10531,
533 2023.
- 534 Yutong He, Naoki Murata, Chieh-Hsin Lai, Yuhta Takida, Toshimitsu Uesaka, Dongjun Kim, Wei-
535 Hsiang Liao, Yuki Mitsufuji, J Zico Kolter, Ruslan Salakhutdinov, et al. Manifold preserving
536 guided diffusion. *arXiv preprint arXiv:2311.16424*, 2023.
537
- 538 Martin Heusel, Hubert Ramsauer, Thomas Unterthiner, Bernhard Nessler, and Sepp Hochreiter. Gans
539 trained by a two time-scale update rule converge to a local nash equilibrium. *Advances in neural*
information processing systems, 30, 2017.

- 540 Jonathan Ho and Tim Salimans. Classifier-free diffusion guidance. *arXiv preprint arXiv:2207.12598*,
541 2022.
- 542
- 543 Yazid Janati, Badr Moufad, Alain Durmus, Eric Moulines, and Jimmy Olsson. Divide-and-conquer
544 posterior sampling for denoising diffusion priors. *Advances in Neural Information Processing*
545 *Systems*, 37:97408–97444, 2024.
- 546 Zahra Kadkhodaie and Eero Simoncelli. Stochastic solutions for linear inverse problems using the
547 prior implicit in a denoiser. *Advances in Neural Information Processing Systems*, 34:13242–13254,
548 2021.
- 549
- 550 Tero Karras, Samuli Laine, and Timo Aila. A style-based generator architecture for generative
551 adversarial networks. In *Proceedings of the IEEE/CVF conference on computer vision and pattern*
552 *recognition*, pp. 4401–4410, 2019.
- 553 Bahjat Kawar, Michael Elad, Stefano Ermon, and Jiaming Song. Denoising diffusion restoration
554 models. *Advances in Neural Information Processing Systems*, 35:23593–23606, 2022a.
- 555
- 556 Bahjat Kawar, Jiaming Song, Stefano Ermon, and Michael Elad. Jpeg artifact correction using
557 denoising diffusion restoration models. *arXiv preprint arXiv:2209.11888*, 2022b.
- 558 Xiang Li, Soo Min Kwon, Shijun Liang, Ismail R Alkhouri, Saiprasad Ravishankar, and Qing Qu.
559 Decoupled data consistency with diffusion purification for image restoration. *arXiv preprint*
560 *arXiv:2403.06054*, 2024.
- 561
- 562 Andreas Lugmayr, Martin Danelljan, Andres Romero, Fisher Yu, Radu Timofte, and Luc Van Gool.
563 Repaint: Inpainting using denoising diffusion probabilistic models. In *Proceedings of the*
564 *IEEE/CVF conference on computer vision and pattern recognition*, pp. 11461–11471, 2022.
- 565 Morteza Mardani, Jiaming Song, Jan Kautz, and Arash Vahdat. A variational perspective on solving
566 inverse problems with diffusion models. *arXiv preprint arXiv:2305.04391*, 2023.
- 567
- 568 Alex Nichol, Prafulla Dhariwal, Aditya Ramesh, Pranav Shyam, Pamela Mishkin, Bob McGrew,
569 Ilya Sutskever, and Mark Chen. Glide: Towards photorealistic image generation and editing with
570 text-guided diffusion models. *arXiv preprint arXiv:2112.10741*, 2021.
- 571 Xinyu Peng, Ziyang Zheng, Wenrui Dai, Nuoqian Xiao, Chenglin Li, Junni Zou, and Hongkai
572 Xiong. Improving diffusion models for inverse problems using optimal posterior covariance. *arXiv*
573 *preprint arXiv:2402.02149*, 2024.
- 574
- 575 Angus Phillips, Hai-Dang Dau, Michael John Hutchinson, Valentin De Bortoli, George Deligiannidis,
576 and Arnaud Doucet. Particle denoising diffusion sampler. *arXiv preprint arXiv:2402.06320*, 2024.
- 577 Ashwini Pople, Matthew J Muckley, Ricky TQ Chen, and Brian Karrer. Training-free linear image
578 inversion via flows. *arXiv preprint arXiv:2310.04432*, 2023.
- 579
- 580 Litu Rout, Yujia Chen, Abhishek Kumar, Constantine Caramanis, Sanjay Shakkottai, and Wen-Sheng
581 Chu. Beyond first-order tweedie: Solving inverse problems using latent diffusion. In *Proceedings*
582 *of the IEEE/CVF Conference on Computer Vision and Pattern Recognition*, pp. 9472–9481, 2024.
- 583 Chitwan Saharia, Jonathan Ho, William Chan, Tim Salimans, David J Fleet, and Mohammad Norouzi.
584 Image super-resolution via iterative refinement. *IEEE transactions on pattern analysis and machine*
585 *intelligence*, 45(4):4713–4726, 2022.
- 586
- 587 Bowen Song, Soo Min Kwon, Zecheng Zhang, Xinyu Hu, Qing Qu, and Liyue Shen. Solving inverse
588 problems with latent diffusion models via hard data consistency. *arXiv preprint arXiv:2307.08123*,
589 2023a.
- 590 Jiaming Song, Chenlin Meng, and Stefano Ermon. Denoising diffusion implicit models. *arXiv*
591 *preprint arXiv:2010.02502*, 2020a.
- 592
- 593 Jiaming Song, Arash Vahdat, Morteza Mardani, and Jan Kautz. Pseudoinverse-guided diffusion
models for inverse problems. In *International Conference on Learning Representations*, 2023b.

- 594 Jiaming Song, Qinsheng Zhang, Hongxu Yin, Morteza Mardani, Ming-Yu Liu, Jan Kautz, Yongxin
595 Chen, and Arash Vahdat. Loss-guided diffusion models for plug-and-play controllable generation.
596 In *International Conference on Machine Learning*, pp. 32483–32498. PMLR, 2023c.
- 597 Yang Song, Jascha Sohl-Dickstein, Diederik P Kingma, Abhishek Kumar, Stefano Ermon, and Ben
598 Poole. Score-based generative modeling through stochastic differential equations. *arXiv preprint*
599 *arXiv:2011.13456*, 2020b.
- 600 Yang Song, Liyue Shen, Lei Xing, and Stefano Ermon. Solving inverse problems in medical imaging
601 with score-based generative models. *arXiv preprint arXiv:2111.08005*, 2021.
- 602 Albert Tarantola. *Inverse problem theory and methods for model parameter estimation*. SIAM, 2005.
- 603 Hengkang Wang, Xu Zhang, Taihui Li, Yuxiang Wan, Tiancong Chen, and Ju Sun. Dmplug: A plug-in
604 method for solving inverse problems with diffusion models. *Advances in Neural Information*
605 *Processing Systems*, 37:117881–117916, 2024.
- 606 Yinhuai Wang, Jiwen Yu, and Jian Zhang. Zero-shot image restoration using denoising diffusion
607 null-space model. *arXiv preprint arXiv:2212.00490*, 2022.
- 608 Luhuan Wu, Brian Trippe, Christian Naesseth, David Blei, and John P Cunningham. Practical and
609 asymptotically exact conditional sampling in diffusion models. *Advances in Neural Information*
610 *Processing Systems*, 36:31372–31403, 2023.
- 611 Lingxiao Yang, Shutong Ding, Yifan Cai, Jingyi Yu, Jingya Wang, and Ye Shi. Guidance with
612 spherical gaussian constraint for conditional diffusion. *arXiv preprint arXiv:2402.03201*, 2024.
- 613 Nebiyou Yismaw, Ulugbek S Kamilov, and M Salman Asif. Gaussian is all you need: A unified
614 framework for solving inverse problems via diffusion posterior sampling. *IEEE Transactions on*
615 *Computational Imaging*, 2025.
- 616 Jiwen Yu, Yinhuai Wang, Chen Zhao, Bernard Ghanem, and Jian Zhang. Freedom: Training-
617 free energy-guided conditional diffusion model. In *Proceedings of the IEEE/CVF International*
618 *Conference on Computer Vision*, pp. 23174–23184, 2023.
- 619 Bingliang Zhang, Wenda Chu, Julius Berner, Chenlin Meng, Anima Anandkumar, and Yang Song.
620 Improving diffusion inverse problem solving with decoupled noise annealing. *arXiv preprint*
621 *arXiv:2407.01521*, 2024.
- 622 Richard Zhang, Phillip Isola, Alexei A Efros, Eli Shechtman, and Oliver Wang. The unreasonable
623 effectiveness of deep features as a perceptual metric. In *Proceedings of the IEEE conference on*
624 *computer vision and pattern recognition*, pp. 586–595, 2018.
- 625 Hongkai Zheng, Wenda Chu, Bingliang Zhang, Zihui Wu, Austin Wang, Berthy T Feng, Caifeng
626 Zou, Yu Sun, Nikola Kovachki, Zachary E Ross, et al. Inversebench: Benchmarking plug-and-play
627 diffusion priors for inverse problems in physical sciences. *arXiv preprint arXiv:2503.11043*, 2025.
- 628 Qinqing Zheng, Matt Le, Neta Shaul, Yaron Lipman, Aditya Grover, and Ricky TQ Chen. Guided
629 flows for generative modeling and decision making. *arXiv preprint arXiv:2311.13443*, 2023.
- 630 Yuanzhi Zhu, Kai Zhang, Jingyun Liang, Jie Zhang Cao, Bihan Wen, Radu Timofte, and Luc Van Gool.
631 Denoising diffusion models for plug-and-play image restoration. In *Proceedings of the IEEE/CVF*
632 *conference on computer vision and pattern recognition*, pp. 1219–1229, 2023.
- 633
634
635
636
637
638
639
640
641
642
643
644
645
646
647

648 A PROOFS

649 A.1 PROOF OF PROP. 3.1.

650 *Proof.* Let $x \equiv x_\epsilon$. The prior and likelihood are

$$651 \quad p(x | x_t) = \mathcal{N}(m_{0|t}, C_{0|t}), \quad p(y | x) = \mathcal{N}(Hx, R),$$

652 with $R = \sigma_y^2 I_m + \sigma_\epsilon^2 H H^\top$. Denote $m := m_{0|t}$ and $C := C_{0|t}$.

653 The posterior is, up to normalization,

$$654 \quad p(x | x_t, y) \propto \exp\left(-\frac{1}{2}(x - m)^\top C^{-1}(x - m) - \frac{1}{2}(y - Hx)^\top R^{-1}(y - Hx)\right).$$

655 Expanding the exponent and collecting terms in x gives

$$656 \quad -\frac{1}{2} \left[x^\top C^{-1} x - 2x^\top C^{-1} m + m^\top C^{-1} m + x^\top H^\top R^{-1} H x - 2x^\top H^\top R^{-1} y + y^\top R^{-1} y \right]$$

$$657 \quad = -\frac{1}{2} \left[x^\top (C^{-1} + H^\top R^{-1} H) x - 2x^\top (C^{-1} m + H^\top R^{-1} y) \right] + (\text{terms independent of } x).$$

658 This is the quadratic form of a Gaussian in x with precision

$$659 \quad \Lambda = C^{-1} + H^\top R^{-1} H,$$

660 and natural parameter

$$661 \quad \eta = C^{-1} m + H^\top R^{-1} y.$$

662 Therefore the posterior is Gaussian $\mathcal{N}(\mu_{\text{post}}, \Sigma_{\text{post}})$ with

$$663 \quad \Sigma_{\text{post}} = \Lambda^{-1} = (C^{-1} + H^\top R^{-1} H)^{-1}, \quad \mu_{\text{post}} = \Sigma_{\text{post}} \eta = (C^{-1} + H^\top R^{-1} H)^{-1} (C^{-1} m + H^\top R^{-1} y).$$

664 Restoring the original notation gives equation 9. \square

665 A.2 PROOF OF EFFICIENT LINEAR SOLVES IN EQ. (38)

666 **Lemma A.1.** Let $H \in \mathbb{R}^{m \times d}$ have (thin) singular-value decomposition $H = U \Sigma V^\top$ with orthogonal
667 $U \in \mathbb{R}^{m \times m}$, $V \in \mathbb{R}^{d \times d}$ and $\Sigma = \text{diag}(s_1, \dots, s_r) \in \mathbb{R}^{m \times d}$, where $r = \text{rank}(H)$ and $s_1 \geq \dots \geq$
668 $s_r > 0$. For any scalars $\eta_1 \geq 0$ and $\eta_2 > 0$ define

$$669 \quad W := \eta_1 H H^\top + \eta_2 \mathbb{I}, \quad Y := \mathbb{I} + H^\top W^{-1} H.$$

670 Then

$$671 \quad W^{-1} = U \text{diag}\left(\frac{1}{\eta_1 s_i^2 + \eta_2}\right)_{i=1}^m U^\top, \quad Y^{-1} = V \text{diag}\left(\frac{1}{1 + s_i^2 / (\eta_1 s_i^2 + \eta_2)}\right)_{i=1}^d V^\top. \quad (14)$$

672 (When $i > r$ we set $s_i = 0$.)

673 *Proof.* (i) **Inverting W .** Using the SVD,

$$674 \quad W = \eta_1 U \Sigma \Sigma^\top U^\top + \eta_2 U \mathbb{I} U^\top = U (\eta_1 \Sigma \Sigma^\top + \eta_2 \mathbb{I}) U^\top.$$

675 Because U is orthogonal, W^{-1} is obtained by inverting the diagonal middle matrix: $(\eta_1 \Sigma \Sigma^\top +$
676 $\eta_2 \mathbb{I})^{-1} = \text{diag}\left(\frac{1}{\eta_1 s_i^2 + \eta_2}\right)_{i=1}^m$. Substituting yields the first identity in equation 14.

677 (ii) **Inverting Y .** Write

$$678 \quad Y = \mathbb{I} + H^\top W^{-1} H = V \Sigma^\top U^\top [U \text{diag}\left(\frac{1}{\eta_1 s_i^2 + \eta_2}\right) U^\top] U \Sigma V^\top + \mathbb{I},$$

679 and simplify with $U^\top U = \mathbb{I}$:

$$680 \quad Y = V \left[\Sigma^\top \text{diag}\left(\frac{1}{\eta_1 s_i^2 + \eta_2}\right) \Sigma + \mathbb{I} \right] V^\top.$$

681 Because $\Sigma^\top \text{diag}\left(\frac{1}{\eta_1 s_i^2 + \eta_2}\right) \Sigma$ is diagonal with i^{th} entry $\frac{s_i^2}{\eta_1 s_i^2 + \eta_2}$, the bracketed matrix is diagonal and
682 hence trivial to invert, giving the second identity in equation 14. \square

A.3 PROOF OF EQ. (6)

Proposition A.2. Let $H \in \mathbb{R}^{m \times d}$, $\eta_1 \geq 0$ and $\eta_2 > 0$. Define

$$W = \eta_1 HH^\top + \eta_2 \mathbb{I}, \quad Y = \mathbb{I} + H^\top W^{-1} H.$$

For any $y \in \mathbb{R}^m$ and $m_{0|t} \in \mathbb{R}^d$ consider the strictly convex quadratic

$$\mathcal{L}(x_0) = \|x_0 - m_{0|t}\|_2^2 + \|y - H\tilde{x}_0\|_{W^{-1}}^2, \quad \|v\|_{W^{-1}}^2 = v^\top W^{-1} v.$$

Its unique minimiser is

$$\tilde{x}_0^* = Y^{-1}[m_{0|t} + H^\top W^{-1} y]. \quad (15)$$

Proof. Expand \mathcal{L} and take its gradient:

$$\nabla_{\tilde{x}_0} \mathcal{L} = 2(\tilde{x}_0 - m_{0|t}) - 2H^\top W^{-1}(y - H\tilde{x}_0).$$

Setting $\nabla_{\tilde{x}_0} \mathcal{L} = 0$ gives the normal equation

$$(\mathbb{I} + H^\top W^{-1} H)\tilde{x}_0 = m_{0|t} + H^\top W^{-1} y, \quad \text{that is, } Y\tilde{x}_0 = m_{0|t} + H^\top W^{-1} y.$$

Because $\eta_2 > 0$ implies $W \succ 0$, we have $W^{-1} \succ 0$ and hence $Y = \mathbb{I} + H^\top W^{-1} H \succ 0$; thus Y is invertible and equation 15 follows.

Finally, the Hessian of \mathcal{L} is $2Y \succ 0$, so \mathcal{L} is strictly convex and the stationary point equation 15 is indeed its unique global minimiser. \square

A.4 PROOF OF REMARK 1.

Proof. As $\eta_2 = 0$,

$$x_0^* = (\eta_1 \mathbb{I} + H^\dagger H)^{-1} (\eta_1 m_{0|t} + H^\dagger y). \quad (16)$$

To analyze the limit as $\eta_1 \rightarrow 0$, decompose the space into two orthogonal components:

- The range (or row space) of H , on which $H^\dagger H$ acts as the identity.
- Its nullspace, on which $H^\dagger H$ is zero.

Let

$$P = H^\dagger H, \quad (17)$$

which is the orthogonal projection onto the row space of H . Then any vector v can be decomposed as

$$v = Pv + (I - P)v. \quad (18)$$

Notice that $H^\dagger y$ lies in the row space (i.e. $P H^\dagger y = H^\dagger y$) and that $m_{0|t}$ can be decomposed as

$$m_{0|t} = P m_{0|t} + (I - P)m_{0|t}. \quad (19)$$

Since the eigenvalues of P are 0 and 1, the matrix $\eta_1 I + P$ has eigenvalues η_1 (on the nullspace of P) and $1 + \eta_1$ (on the row space). Hence, its inverse acts as:

- Multiplication by $1/\eta_1$ on the nullspace,
- Multiplication by $1/(1 + \eta_1)$ on the row space.

Thus, we have

$$(\eta_1 I + P)^{-1} (H^\dagger y + \eta_1 m_{0|t}) = \frac{1}{1 + \epsilon} (H^\dagger y + \eta_1 P m_{0|t}) + \frac{1}{\eta_1} (\eta_1 (I - P)m_{0|t}). \quad (20)$$

Simplify this to obtain

$$\frac{1}{1 + \eta_1} H^\dagger y + \frac{\eta_1}{1 + \eta_1} P m_{0|t} + (I - P)m_{0|t}. \quad (21)$$

Now, taking the limit as $\eta_1 \rightarrow 0$:

- $\frac{1}{1+\eta_1} \rightarrow 1$,
- $\frac{\eta_1}{1+\eta_1} \rightarrow 0$.

Therefore, the limit becomes

$$\lim_{\eta_1 \rightarrow 0} x_0^* = H^\dagger y + (I - P)m_{0|t}. \quad (22)$$

Recalling that $P = H^\dagger H$, we rewrite this as

$$H^\dagger y + m_{0|t} - H^\dagger H m_{0|t} = m_{0|t} + H^\dagger (y - H m_{0|t}). \quad (23)$$

Thus, in the limit where $\eta_1 \rightarrow 0$, we indeed have

$$x_0^* = m_{0|t} + H^\dagger (y - H m_{0|t}). \quad (24)$$

This shows that, as the relative measurement noise ϵ becomes much smaller compared to the prior uncertainty r_t , the posterior expectation is the projection of \hat{x}_0^θ onto the subspace $\{x : Hx = y\}$. \square

B ADDITIONAL METHOD DETAILS

B.1 ADDRESSING GAUSSIAN NOISE

Consider noisy image restoration problems in the form of $y = Hx + \epsilon_y$, where ϵ_y is the added noise. Then the measurement y can be decomposed to the sum of clean measurement $y^{\text{clean}} := Hx$ and measurement noise ϵ_y . Calculating x_0^* leads to:

$$x_0^* = Y^{-1}[m_{0|t} + H^\top W^{-1}y] \quad (25)$$

$$= m_{0|t} + (Y^{-1} - \mathbb{I})m_{0|t} + Y^{-1}H^\top W^{-1}y \quad (26)$$

where $Y^{-1}H^\top W^{-1}\epsilon_y$ is the extra noise introduced into x_0^* and will be further introduced into $x_{t-\Delta t}$.

To address Gaussian noise with known variance, we modify Eq. (7) and Eq. (2) as:

$$x_0^* = m_{0|t} + \Sigma_t[(Y^{-1} - \mathbb{I})m_{0|t} + H^\top W^{-1}y] \quad (27)$$

$$x_{t-\Delta t} \sim \mathcal{N}(a_t \tilde{x}_0^{\text{pe}}(t, x, y) + b_t x_t, \Phi_t \mathbb{I}) \quad (28)$$

Then x_0^* is:

$$x_0^* = m_{0|t} + \Sigma_t[(Y^{-1} - \mathbb{I})m_{0|t} + H^\top W^{-1}y] \quad (29)$$

$$(30)$$

$$= \underbrace{m_{0|t} + \Sigma_t(Y^{-1} - \mathbb{I})m_{0|t} + Y^{-1}H^\top W^{-1}y^{\text{clean}}}_{:= \tilde{x}_0^{\text{clean}}} + \Sigma_t Y^{-1}H^\top W^{-1}\epsilon_y \quad (31)$$

Then the iteration of the sampling process is:

$$x_{t-\Delta t} = a_t x_0^*(t, x, y) + b_t x_t + \epsilon_{\text{new}}, \quad \epsilon_{\text{new}} \sim \mathcal{N}(0, \Phi_t) \quad (32)$$

$$= a_t \tilde{x}_0^{\text{clean}} + b_t x_t + \underbrace{a_t \sigma_y Y^{-1}H^\top W^{-1}\epsilon_y}_{:= \epsilon_{\text{intro}}} + \epsilon_{\text{new}} \quad (33)$$

Suppose $\Sigma_t = V \text{diag}\{\lambda_{t1}, \dots, \lambda_{td}\} V^T$, $\Phi_t = V \text{diag}\{\gamma_{t1}, \dots, \gamma_{td}\} V^T$. Then the introduced noise $\epsilon_{\text{intro}} = a_t \sigma_y Y^{-1} H^T W^{-1} \epsilon_y$ is still a Gaussian distribution: $\epsilon_{\text{intro}} \sim \mathcal{N}(0, V D_t V^T)$, with $D_t = \text{diag}\{d_{t1}, \dots, d_{td}\}$:

$$d_{ti} = \begin{cases} \frac{a_t^2 \sigma_y^2 s_i^2 \lambda_{ti}^2}{[(\eta_1 + 1) s_i^2 + \eta_2]^2}, & s_i \neq 0, \\ 0, & s_i = 0, \end{cases} \quad (34)$$

The choice of Φ_t need to ensure the total noise injected to $x_{t-\Delta t}$ conforms the iteration in Eq. (2).

$$\epsilon_{\text{new}} + \epsilon_{\text{intro}} \sim \mathcal{N}(0, c_t^2 \mathbb{I}) \quad (35)$$

To construct ϵ_{new} , we define a new diagonal matrix $\Gamma_t (= \text{diag}\{\gamma_{t1}, \dots, \gamma_{td}\})$:

$$\gamma_{ti} = \begin{cases} c_t^2 - \frac{a_t^2 \sigma_y^2 s_i^2 \lambda_{ti}^2}{[(\eta_1 + 1) s_i^2 + \eta_2]^2}, & s_i \neq 0, \\ c_t^2, & s_i = 0, \end{cases} \quad (36)$$

Now we can yield ϵ_{new} by sampling from $\mathcal{N}(0, V \Gamma_t V^T)$ to ensure that $\epsilon_{\text{intro}} + \epsilon_{\text{new}} \sim \mathcal{N}(0, c_t^2 \mathbb{I})$. We need to make sure λ_{ti} guarantees the noise level of the introduced noise does not exceed the pre-defined noise level c_t , we also hope λ_{ti} as close as 1 as possible. Therefore,

$$\lambda_{ti} = \begin{cases} 1, & c_t \geq \frac{a_t \sigma_y s_i}{(\eta_1 + 1) s_i^2 + \eta_2}, \\ \frac{c_t ((\eta_1 + 1) s_i^2 + \eta_2)}{a_t \sigma_y s_i}, & c_t < \frac{a_t \sigma_y s_i}{(\eta_1 + 1) s_i^2 + \eta_2}, \\ 1, & s_i = 0. \end{cases} \quad (37)$$

In practice, we found that setting σ_y slightly larger than the true σ_y is beneficial, possibly because the denoiser is more sensitive to excessive noise.

B.2 EFFICIENT CALCULATION VIA SVD DECOMPOSITION

Let $H = U \Sigma V^T$ with singular values s_1, \dots, s_n . Then

$$W^{-1} = U \text{diag}\left(\frac{1}{\eta_1 s_i^2 + \eta_2}\right) U^T, \quad Y^{-1} = V \text{diag}\left(\frac{1}{1 + s_i^2 / (\eta_1 s_i^2 + \eta_2)}\right) V^T, \quad (38)$$

see Sec. A for the proof. Hence both $W^{-1}v$ and $Y^{-1}u$ reduce to inexpensive diagonal scalings in the SVD basis, avoiding the calculation of any explicit matrix inversion or square-root. The algorithm of MAS for inverse problem is provided in Algorithm 1.

As $\eta_1 < 0$, W could be non-invertible. However, $W = U \text{diag}(\eta_1 s_1^2, \dots, \eta_1 s_r^2, \eta_2, \dots, \eta_2) U^T$. Hence W is invertible if $\eta_1 s_i^2 + \eta_2 \neq 0$ for every i . Even when $\eta_2 = 0$ and $\eta_1 < 0$ make W singular, the update $W^\dagger y$ uses the Moore-Penrose pseudo-inverse W^\dagger , which is always well-defined. The pseudo-inverse acts like an ordinary inverse on the range of H and leaves the null-space untouched, so the sampler remains stable. Empirically, small negative values ($-0.5 < \eta_1 < 0$) often give the visual boost without instability, as demonstrated in the ablation studies in Sec. 5

Why a negative η_1 value leads to improvements? As $\eta_2 = 0$, x_0^* in Eq. (7) can be rewritten as:

$$x_0^* = m_{0|t} + \frac{1}{1 + \eta_1} H^\dagger (y - H m_{0|t}) = m_{0|t} + \frac{1}{1 + \eta_1} (x_0^{\text{proj}} - m_{0|t}) \quad (39)$$

where

$$x_0^{\text{proj}} := m_{0|t} + H^\dagger y - H^\dagger H m_{0|t} \quad (40)$$

is the the orthogonal projection of $m_{0|t}$ onto the affine constraint set $\{x : Hx = y\}$. Thus, the update direction $x_0^{proj} - m_{0|t}$ plays the role of a guidance direction, and the scalar $1/(1 + \eta_1)$ acts as guidance strength. When $\eta_1 < 0$, we have $1/(1 + \eta_1) > 1$, i.e., a step larger than the projection step. Such over-guidance (guidance scale > 1) is well-documented in diffusion literature: in particular, Ho & Salimans (2022) and Nichol et al. (2021) all show that over-guidance (scale > 1) improves perceptual fidelity and conditioning strength, at the cost of reduced diversity. Our use of $\eta_1 < 0$ mirrors this phenomenon: a stronger measurement-consistent pull improves reconstruction fidelity under model mismatch, despite departing from the strict probabilistic interpretation.

B.3 ADDRESSING UNKNOWN NOISE AND NON-DIFFERENTIABLE MEASUREMENTS

As the measurement noise ϵ_y is non-Gaussian or unknown, it’s difficult to ensure the total noise introduced in $x_{t-\Delta t}$ is $\mathcal{N}(0, c_t^2 \mathbb{I})$. In this case, we calculate x_0^* using Eq. (7) and update $x_{t-\Delta t}$ using Eq. (2). Then x_0^* is:

$$x_0^* = m_{0|t} + [(Y^{-1} - \mathbb{I})m_{0|t} + H^T W^{-1} y] \quad (41)$$

$$= m_{0|t} + (Y^{-1} - \mathbb{I})m_{0|t} + Y^{-1} H^T W^{-1} y^{\text{clean}} + Y^{-1} H^T W^{-1} \epsilon_y \quad (42)$$

$$= \underbrace{m_{0|t} + (Y^{-1} - \mathbb{I})m_{0|t} + Y^{-1} H^T W^{-1} y^{\text{clean}}}_{:= \tilde{x}_0^{\text{clean}}} + Y^{-1} H^T W^{-1} \epsilon_y \quad (43)$$

where $Y^{-1} H^T W^{-1} \epsilon_y$ is the extra noise introduced into x_0^* and will be further introduced into $x_{t-\Delta t}$:

$$\begin{aligned} x_{t-\Delta t} &= a_t x_0^* + b_t x_t + \epsilon_{\text{new}}, \\ &= a_t \tilde{x}_0^{\text{clean}} + b_t x_t + \underbrace{a_t Y^{-1} H^T W^{-1} \epsilon_y}_{:= \epsilon_{\text{intro}}} + \epsilon_{\text{new}}, \end{aligned} \quad (44)$$

where ϵ_{new} the noise added by diffusion process, which should be specifically designed to ensure $x_{t-\Delta t}$ is sampled from correct distribution as in Eq. (2), i.e., the total noise $\epsilon_{\text{intro}} + \epsilon_{\text{new}} \sim \mathcal{N}(0, c_t^2 \mathbb{I})$. However, as ϵ_y is unknown noise, we have no information about the introduced noise ϵ_{intro} . To solve this problem, we made the following principles: (i) despite that fact that we cannot guarantee $\epsilon_{\text{intro}} + \epsilon_{\text{new}} \sim \mathcal{N}(0, c_t^2 \mathbb{I})$, we still hope $\epsilon_{\text{intro}} + \epsilon_{\text{new}}$ is as close to $\mathcal{N}(0, c_t^2 \mathbb{I})$ as possible; (ii) small η_1 and η_2 are helpful to maximize the alignment to measurement y . Notably,

$$\epsilon_{\text{intro}} = a_t Y^{-1} H^T W^{-1} \epsilon_y \quad (45)$$

$$= a_t V \text{diag} \left(\frac{s_i}{(\eta_1 + 1) s_i^2 + \eta_2} \right) U^T \epsilon_y \quad (46)$$

η_1 and η_2 are two variables that control the noise level of ϵ_{intro} . In the implementation, we still sample ϵ_{new} from Gaussian distribution $\mathcal{N}(0, c_t^2 \mathbb{I})$. Then the problem becomes how to select η_1 and η_2 to meet the above 2 principles. For common image restoration tasks like SR, Deblurring, inpainting, Colorization, The maximum eigenvalue value $s_{\text{max}} = \max\{s_i\} \leq 1$. Therefore, adjusting η_2 is more likely to reduce the strength of ϵ_{intro} .

Principle (i): Control the deviation from Gaussian reverse noise. Let

$$A_t = \frac{a_t}{c_t} V \text{diag} \left(\frac{s_i}{(\eta_1 + 1) s_i^2 + \eta_2(t)} \right) U^T, \quad \frac{\epsilon_{\text{intro}}}{c_t} = A_t \epsilon_y.$$

To make the total noise

$$\frac{\epsilon_{\text{intro}}}{c_t} + \frac{\epsilon_{\text{new}}}{c_t}$$

as close as possible to $\mathcal{N}(0, \mathbb{I})$, we require the operator norm of A_t to be uniformly bounded:

$$\|A_t\|_2 = \max_i \left| \frac{a_t}{c_t} \frac{s_i}{(\eta_1 + 1) s_i^2 + \eta_2(t)} \right| \leq C. \quad (\text{P1})$$

Since $s_i \leq s_{\max}$, this condition is satisfied if $\eta_2(t) \geq k a_t/c_t$, which implies

$$\|A_t\|_2 \leq \frac{s_{\max}}{k}.$$

Principle (ii): Preserve measurement alignment. To preserve measurement alignment, we require η_1 and η_2 as small as possible, Considering $\eta_2(t) \geq k a_t/c_t$, the solution to meet Principle (ii) is exactly $\eta_2(t) = k a_t/c_t$, where k is a constant that limit A_t to be uniformly bounded.

C LIMITATIONS

While MAS can, in principle, be generalized to nonlinear inverse problems, explicitly formulating the likelihood term $p(y | x_\ell)$ becomes challenging. Developing effective sampling techniques under this setting is a promising direction for future research.

D IMPACT STATEMENT

Our method can improve image restoration under challenging noise and degradation conditions, which may benefit applications in medical imaging, scientific visualization, cultural heritage preservation, and general photography. However, it is important to note that as with many generative and restoration models, our method could be misused for malicious image manipulation.

E PYTORCH-LIKE CODE IMPLEMENTATION

Here we provide a basic PyTorch-Like implementation of the calculation of x_0^* in Eq. (7), shown in Listing 1.

Listing 1 PyTorch-like implementation of the calculation of x_0^* in Eq. (7).

```

946 1 @torch.no_grad()
947 2 def mas(
948 3     H, x0_hat, y,
949 4     eta_1=-0.2, eta_2=0.0
950 5 ):
951 6     bs, _, H_img, W_img = x0_hat.shape
952 7     x0_hat = x0_hat.view(bs, -1)
953 8     y           = y.view( bs, -1)           # measurement dim m
954 9     ut_y       = H.Ut(y)                   # (bs, m)
955 10    singulars   = H.singulars()              # (m,)
956 11    nz         = singulars > 0               # boolean mask
957 12    scale1     = 1.0 / (singulars[nz] ** 2 * eta_1 + eta_2)
958 13    ut_y[:, nz] = ut_y[:, nz] * scale1       # broadcasting OK
959 14    u_y       = H.U(ut_y)                   # (bs, m)
960 15    rhs      = x0_hat + H.Ht(u_y)           # (bs, d)
961 16
962 17    vt_rhs    = H.Vt(rhs)                   # (bs, d)
963 18    scale2    = 1.0 / (1.0 + singulars[nz]**2 / (singulars[nz]**2 *
964 19    ↪ eta_1 + eta_2))
965 20    vt_rhs[:, nz] = vt_rhs[:, nz] * scale2
966 21    x0_pm     = H.V(vt_rhs)                 # (bs, d)
967 22    x0_pm     = x0_pm.view(bs, 3, H_img, W_img)
968 23    return x0_pm

```

F EXPERIMENTAL DETAILS

F.1 DETAILS OF THE DEGRADATION OPERATORS

Super-resolution. We use the downsampler with bicubic kernel as the forward operator.

Table 5: Sampling time (Sec) per image of MAS on deblurring and super-resolution with FFHQ 256, evaluated using a single NVIDIA A6000 48G GPU. We set NFE=20 and batch size = 20 for all of the methods.

Method	MAS	IIGDM	DDNM	DDRM	RED-Diff
Deblurring	0.128	0.278	0.127	0.127	0.119
SR (8×)	0.131	0.282	0.131	0.131	0.125

Table 6: Ablation study of k for solving JPEG restoration and Quantization.

Method	k	JPEG Restoration (QF = 5)				JPEG Restoration (QF = 2)				Quantization (number of bits = 2)			
		PSNR ↑	SSIM ↑	LPIPS ↓	FID ↓	PSNR ↑	SSIM ↑	LPIPS ↓	FID ↓	PSNR ↑	SSIM ↑	LPIPS ↓	FID ↓
IIGDM	-	25.78	0.750	0.241	89.82	22.92	0.653	0.314	112.27	29.98	0.823	0.185	124.57
	0.5	26.00	0.778	0.317	122.56	22.64	0.653	0.485	264.82	28.97	0.837	0.196	69.62
MAS (ours)	1.0	26.30	0.787	0.281	101.27	23.29	0.698	0.409	164.54	28.44	0.826	0.196	75.09
	2.0	25.97	0.774	0.273	103.09	23.75	0.722	0.351	119.86	27.22	0.798	0.220	89.94
	3.0	25.41	0.758	0.281	106.71	23.72	0.722	0.335	114.81	26.23	0.776	0.243	96.86

Deblurring. For deblurring experiments, We use uniform blur kernel to to implement blurring operation.

Inpaint (Random). Random Inpainting uses a generated random mask where each pixel has a 70% chance of being masked, following the settings in (Song et al., 2023a).

Inpaint (box). We use a fixed square mask of size 128×128 pixels placed at the center of the image.

Colorization. We simulate grayscale degradation by applying a fixed linear transformation to each pixel using the matrix $[\frac{1}{3}, \frac{1}{3}, \frac{1}{3}]$, replacing each RGB pixel with its average intensity.

F.2 DETAILS OF THE BASELINE MODELS

Sampler. Most experiments on diffusion models leverage DDIM (Song et al., 2020a) sampling.

DDRM (Kawar et al., 2022a). $\eta_B = 1.0$, $\eta = 0.85$ with DDIM sampler, as advised in the original paper.

IIGDM (Song et al., 2023b). $\eta = 1.0$, with DDIM sampler, as advised in the original paper.

Reddiff (Mardani et al., 2023). $\lambda = 0.25$, with DDIM sampler, as advised in the original paper.

DDNM (Wang et al., 2022). $\eta = 0.85$, with DDIM sampler, as advised in the original paper.

DAPS (Zhang et al., 2024). $\tau = 0.01$, with EDM sampler, as advised in the original paper.

G ADDITIONAL RESULTS

G.1 COMPUTATIONAL TIME

The computational time of MAS on solving inverse problems is shown in Table 5. Our model achieves similar efficiency to DDNM and DDRM, demonstrating that MAS introduces minimal overhead while maintaining competitive runtime performance.

G.2 ABLATION STUDY OF k

We perform an ablation study of the parameter k for JPEG restoration and quantization (see Table 6). The results indicate that our method is robust to the choice of k , and a single setting (e.g., $k = 1$) provides consistently strong performance across all three degradations. Importantly, in contrast to IIGDM, MAS operates without requiring access to the forward operator.



Figure 6: Super-resolution restoration over various strength of degradation. We set $\eta_1 = -0.4$ and $\eta_2 = 0$ for all tasks. For sampling process, we set $\eta = 0.6$.

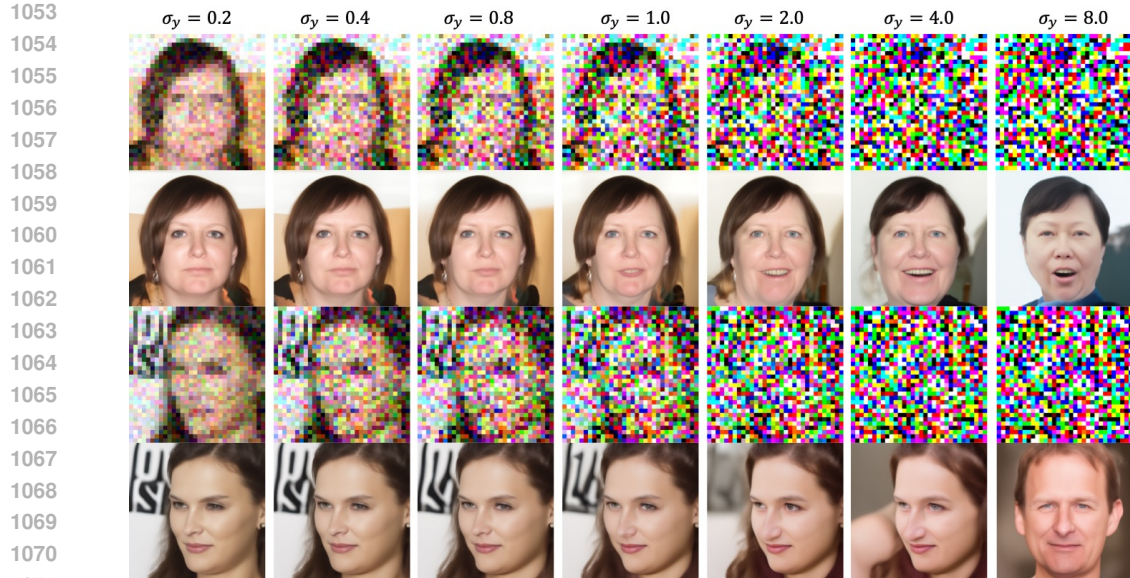
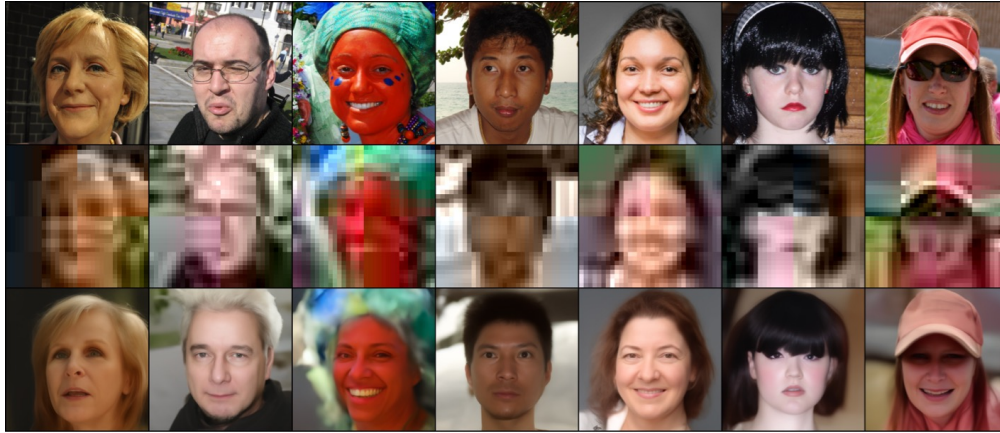


Figure 7: MAS for solving super-resolution ($8\times$) with various strength of Gaussian noise.

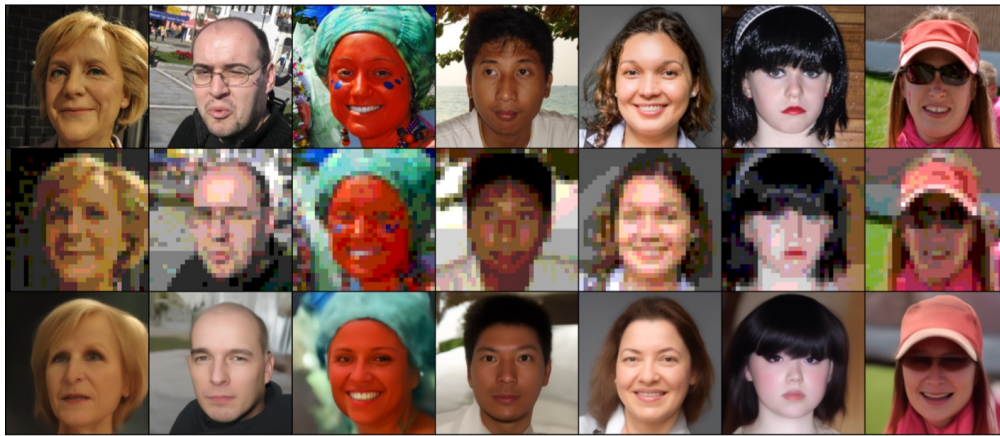
G.3 ADDING GAUSSIAN NOISE

We present the results of solving $8\times$ super-resolution under varying levels of Gaussian noise in Fig. 7. The visualizations demonstrate that MAS maintains strong restoration performance, even under high noise conditions.

1080
 1081
 1082
 1083
 1084
 1085
 1086
 1087
 1088
 1089
 1090
 1091
 1092
 1093
 1094
 1095
 1096
 1097
 1098
 1099
 1100
 1101
 1102
 1103
 1104
 1105
 1106
 1107
 1108
 1109
 1110
 1111
 1112
 1113
 1114
 1115
 1116
 1117
 1118
 1119
 1120
 1121
 1122
 1123
 1124
 1125
 1126
 1127
 1128
 1129
 1130
 1131
 1132
 1133



(a) SR(8×) + JPEG



(b) SR (8×) + Quantization

Figure 8: Additional visualization of super-resolution with unknown noise.

G.4 ADDING NON-DIFFERENTIABLE DEGRADATION

We present the results of solving $8\times$ super-resolution with non-differentiable degradations, including JPEG compression and quantization, in Fig. 8.

H LICENSES

FFHQ Dataset. We use the Flickr-Faces-HQ (FFHQ) dataset released by NVIDIA under the Creative Commons BY-NC-SA 4.0 license. The dataset is intended for non-commercial research purposes only. More details are available at: <https://github.com/NVlabs/ffhq-dataset>.

ImageNet Dataset. The ImageNet dataset is used under the terms of its academic research license. Access requires agreement to ImageNet’s data use policy, and redistribution is not permitted. More information is available at: <https://image-net.org/download>.